Doubly excited pulse waves on thin liquid films flowing down an inclined plane: An experimental and numerical study

Idris Adebayo,[1] Zhihua Xie,[1,2] Zhizhao Che,[1,3] and Omar K. Matar[1]
[1]*Department of Chemical Engineering, Imperial College London, SW7 2AZ, United Kingdom*
[2]*School of Engineering, Cardiff University, Cardiff, CF24 3AA, United Kingdom*
[3]*State Key Laboratory of Engines, Tianjin University, Tianjin, People's Republic of China*
(Received 27 February 2017; revised manuscript received 20 April 2017; published 27 July 2017)

The interaction patterns between doubly excited pulse waves on thin liquid films flowing down an inclined plane are studied both experimentally and numerically. The effect of varying the film flow rate, interpulse interval, and substrate inclination angle on the pulse interaction patterns is examined. Our results show that different interaction patterns exist for these binary pulses, which include solitary wave behavior, partial or complete pulse coalescence, and pulse noncoalescence. A regime map of these patterns is plotted for each inclination angle examined, parametrized by the film Reynolds number and interpulse interval. Finally, the individual effect of the system parameters mentioned above on the coalescence distance of binary pulses in the "complete pulse coalescence" mode is studied; the results are compared to numerical simulations of the two-dimensional Navier-Stokes equations yielding good agreement.

DOI: 10.1103/PhysRevE.96.013118

I. INTRODUCTION

Thin flowing films play a key role in the design and efficient maintenance of many types of process equipment in industry. These include reactors, condensers, cooling systems, distillation towers, etc. [1]. Their application is chiefly seen in the intensification of both heat and mass transfer at the film interface and wall [2,3]. Other fields of application include nanofluidics, microfluidics, coating flows, lava flows, dynamics of continental ice sheets, tear-film rupture, and surfactant replacement therapy; this demonstrates that their importance is not only limited to engineering settings, but also extends to cover geophysics, as well as biophysics [4]. Hence it is important to achieve a fundamental understanding of the complex film dynamics to enable their manipulation and control. In this paper, we focus our attention on the dynamics of forced, thin films, flowing down an inclined plane with significant inertia.

Many researchers have made significant contributions to the area of falling films, and films flowing down inclined planes, from the standpoint of experiments, theory, modeling, and simulation. Pioneering experimental work was carried out by Kapitza and Kapitza [5] who studied the evolution of waves on thin films in the film Reynolds number range of 7–23. Gollub and co-workers [6,7] also carried out extensive studies on the development of large-amplitude solitary waves with front-running capillary waves. They investigated the secondary instabilities following the initial bifurcation from a flat film steady state, and showed the evolution of so-called "herringbone" patterns from two-dimensional waves due to a subharmonic instability, and a synchronous three-dimensional mode arising from a sideband instability. They also made predictions about the coalescence of solitary waves, which form a major focus of the present study. Park and Nosoko [8] also studied the transverse evolution of solitary waves in a vertically falling water film for film Reynolds numbers in the range 10–100. They controlled the wavelength of transverse perturbations using needles, put in contact with the film free surface, and discovered a critical perturbation wavelength for solitary wave stability.

Nosoko *et al.* [9] investigated wave characteristics in the film Reynolds number range 14–90 and derived correlations for the dependence of both wave speed and peak height on the wavelength as well as the film Reynolds and Weber numbers. Nosoko and Miyara [10] also studied wave evolution dynamics over a similar range of parameters and showed that inlet disturbances of low frequencies usually grow into solitary waves, while sinusoidal waves are formed at high frequencies. They also demonstrated the difference between naturally formed and forced waves in terms of wave shapes and the kinematics. More recently, Kofman *et al.* [11] investigated the stability of solitary waves, with emphasis on the effect of the inclination angle on secondary instabilities and the resultant three-dimensional patterns.

From the standpoint of mathematical modeling, linear stability analyses of the base state of thin film flows were first conducted by Yih [12,13] and Benjamin [14]. They showed this base state to be unstable to long-wavelength disturbances. Since then, simplified equations have been developed by Benney [15], Shkadov [16], Yu *et al.* [17], Nguyen and Balakotaiah [18], amongst many others [4,19–21], from the full Navier-Stokes equations by a long-wave approximation and with different order-of-magnitude assumptions for the important Re and We numbers. The agreement of the results obtained with experimental data has also gotten better. In terms of numerical simulations, Alekseenko *et al.* [22] simulated the evolution of wavy films by solving an integral boundary layer equation and compared their results with their experimental data. Miyara [23] carried out a direct numerical simulation of the wavy film using the simplified marker and cell method. The drawback to this method, however, is the increased computational requirement, especially in three-dimensional simulations. Gao *et al.* [24] also performed numerical simulations of wavy falling film flows on vertical planes

focusing on the development of both sinusoidal and solitary wave families at film Reynolds numbers below 70. In addition to the inelastic collisions between two solitary waveforms predicted by Liu and Gollub [6], Chang *et al.* [25] also predicted the possible formation of bounded pairs of double-hump pulses as a result of a balance between the attractive and repulsive interactions of solitary waves; the details of these interactions are examined in the present study.

More recent work focusing on the interactions between solitary waves include the analysis of the interaction patterns between nonlinear pulses carried out by Tseluiko *et al.* [26]. They utilized a weak-interaction theory for solitary pulses of the generalized Kuramoto-Sivashinsky equation and studied the inelastic collision between droplike solitary pulses. They also provided evidence of the formation of bound states of groups of pulses in which the pulses travel with the same velocities as a whole. Pradas *et al.* [27] also studied the dynamics associated with bound states in a falling liquid film. They applied a coherent-structure theory which also predicted the bound-state formation in the interaction of these solitary pulses.

In summary, the studies in the literature have considered either naturally evolving, or artificially excited waves [4,19–21,28]. "Natural" waves are formed as a result of amplification of infinitesimal disturbances at the inlet [29], while "forced" waves are produced via the imposition of inlet frequency forcing, which ensures that waves that exhibit regular spatiotemporal dynamics are obtained on the film [6,30]. Depending on the forcing frequency, two types of waves are observed: the so-called γ_1 and γ_2 waves [21,31]; the former are sinusoidal-like, and the latter are characterized by solitary, large-amplitude humps having long tails and steep fronts, with front-running capillary waves. The γ_2 waves are fast moving and exhibit inelastic collision with other waves; their speed is also a function of the frequency and amplitude [6,7,20,32].

Despite the abundance of studies in the literature on the wave evolution dynamics of flowing liquid films, however, the interaction patterns between isolated, excited binary pulse waves on a naturally developing film have not received much attention. This is important from the viewpoint of "dissecting" complex wave interactions, which lead to interfacial "turbulence," and a necessary precursor to the development of control strategies for thin flowing films with large inertial contributions. In this work, we present a detailed analysis of the behavior of doubly excited planar pulse waves on an adjustable inclined glass substrate with varying liquid film flow rates, and interpulse intervals. The different patterns obtained are carefully scrutinized, and the factors and mechanisms underlying their formation are also studied. The interaction patterns are examined by means of numerical simulations of the Navier-Stokes equations whose predictions are compared with the experimental results. The outcome of this work will improve our understanding of the interaction patterns between waveforms on flowing liquid films.

The rest of this paper is organized as follows. The experimental system is described in Sec. II, including the falling film rig, the pulse-wave excitation unit, and the high-speed imaging system. The numerical setup is shown in Sec. III while both experimental and numerical results are presented in Sec. IV; a regime map of the various interaction patterns is also shown here. Finally, concluding remarks are provided in Sec. V.

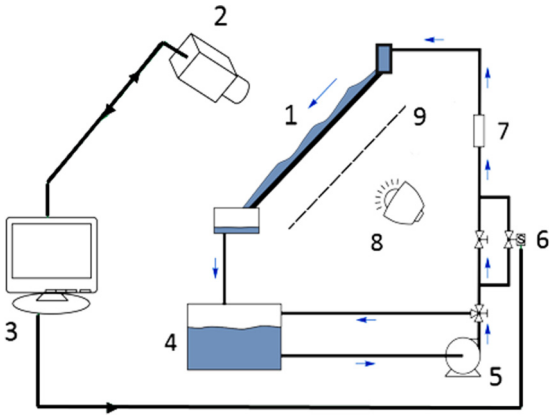

FIG. 1. Schematic of the experimental setup for doubly excited pulse waves on flowing liquid films, comprising the falling film rig, and a pulse-excitation and high-speed imaging system. The items are 1: glass substrate; 2: high-speed camera; 3: computer; 4: reservoir tank; 5: pump; 6: solenoid valve; 7: ultrasonic flow meter; 8: halogen lamp; 9: light diffuser.

II. EXPERIMENTAL METHOD

A. Falling liquid film

The experimental setup used to study the doubly excited pulse waves is shown in Fig. 1. An ultrasonic flowmeter (Cynergy3 UF25B, RS Components UK) was used to measure the liquid flow rate with a range of flow between 0.5 and 25 l/min. The substrate inclination was varied between 5° and 15°, while the film Reynolds number, $\mathrm{Re} = \rho_w q/w\mu_w$, ranged between 55.5 and 166.5, so as to adequately capture the full range of interaction patterns between the excited pulses: from solitary wave behavior, to complete pulse coalescence. Here, ρ_w and μ_w denote the density and viscosity of the test liquid (de-ionized water), which are 1000 kg/m^3 and 10^{-3} Pa s, respectively, while q and w are the flow rate and width of the falling liquid film, respectively. In comparison with air, the density ratio ρ_w/ρ_a is 889. The range of the inverse Weber number, $\mathrm{We} = \sigma/\rho_w h_N u_N^2$, was between 1.5 and 13.5, while the critical Re number $\mathrm{Re}_c = \frac{5}{4}\cot\beta$ [14] for wave growth was in the range 4.7–14.3 for the inclination angles examined (i.e., $\beta = 5°, 10°$, and 15°); see Table I for the definition of h_N and u_N, which denote the Nusselt film thickness and velocity, respectively, and the ranges of all the physical parameters relevant to the present flow. Finally, the Kapitza number, $\mathrm{Ka} = \sigma\rho^{1/3}/g^{1/3}\mu^{4/3}$, for de-ionized water was 3363.

B. Pulse excitation

A solenoid valve (SMC VXD series pilot operated, two port) was used to excite the binary pulses. It was connected to the primary circuit downstream from the flow rate control valve and in addition to a bypass around it. The purpose of the bypass was to ensure that film flow is sparsely maintained on the substrate even when the solenoid valve is shut. A ball valve is used to control the amount of flow through the bypass, while the solenoid valve itself is made to receive the pulse-wave signals from a data acquisition card (National Instrument DAQ, UK) via a nonlatching relay (Takamisawa A5W-K). A MATLAB

TABLE I. List of experimental and numerical parameters.

Variables	Definition	Value/range	Units
Nusselt film thickness	$h_N = \left(\frac{3\mu_w^2 \mathrm{Re}}{\rho_w^2 g \sin\beta}\right)^{1/3}$	$(4.034 - 8.363) \times 10^{-4}$	m
Nusselt velocity	$u_N = \frac{\rho_w g \sin\beta h_N^2}{3\mu_w}$	0.0957−0.2862	m/s
Perturbed film velocity	u_p	0.1914−0.5724	m/s
Gravitational acceleration	g	9.81	m/s^2
Inclination angle	β	5°−15°	deg
Liquid density	ρ_w	1000	kg/m^3
Liquid viscosity	μ_w	1.0×10^{-3}	Pa s
Air density	ρ_a	1.125	kg/m^3
Air viscosity	μ_a	1.81×10^{-5}	Pa s
Surface tension	σ	0.072	N/m
Film Reynolds number	$\mathrm{Re} = \rho_w q / w \mu_w$	55.5−166.5	
Film inverse Weber number	$\mathrm{We} = \sigma / \rho_w h_N u_N^2$	1.5−13.5	
Kapitza number	$\mathrm{Ka} = \sigma \rho^{1/3} / g^{1/3} \mu^{4/3}$	3363	

routine was used to communicate with the DAQ card and this had the capability of adjusting different parameters on the output signal including frequency, amplitude, and interpulse time spacing, as desired. The output signal, as shown in Fig. 2, was simply translated into the opening and closing of the valve by the relay. The interpulse time spacing B was varied between 0.04 and 0.12 s while the pulse duration A was maintained at 0.04 s; T is the pulse period, measured in seconds, as shown in Fig. 2.

C. High-speed imaging

An Olympus i-SPEED 3 camera was used for high-speed imaging in conjunction with two separate lenses: a Sigma 105 mm $f/2.8$ Macro Ex lens, and a Nikon 60 mm $f/2.8$ D lens. The first lens was used to take full-scale images of the film structure, while the second was used to take images of specific regions of the film surface. The camera was placed at a right angle to the film surface, so as to ensure a sharp focus of the complete film surface was obtained. A central position was also maintained in the spanwise direction, to minimize potential boundary effects from the substrate edges. The camera was used mainly at 1000 frames per second, 800 × 600 resolution, and a shutter speed of 1 ms. Illumination was maintained by means of a halogen lamp used with a light diffuser. The high-speed images acquired were then analyzed using a customized MATLAB program from which the space-time plots were generated. The MATLAB routine transforms information on each of the image sequences recorded in the experiment by converting the data on each time instant of the recording into a two-dimensional matrix; it then plots the evolution and propagation of the pulse waves with the location of a wave shown in the streamwise direction, and the corresponding time in the transverse direction.

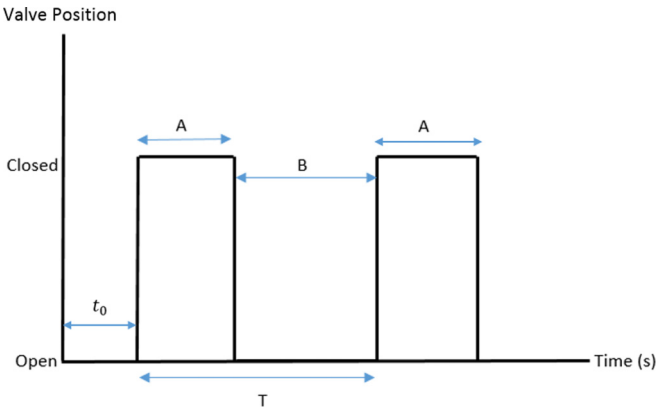

FIG. 2. Generated pulse-wave excitation signal for valve control: A is the pulse duration, B is the interpulse interval, T is the period of the pulse, and t_0 is the interval prior to wave excitation.

III. NUMERICAL SIMULATION

A. Governing equations

We assume the two components (air and water) exist as a single phase, and then define their respective mass fractions as α_i for component i. Thus we enforce a mass constraint on the system as

$$\sum_{i=1}^{N_c} \alpha_i = 1, \tag{1}$$

where N_c is the number of components, which equals 2 in the present case (with subscript i being a for air and w for water). For incompressible and isothermal flow, the conservation of mass for each fluid (air and water) is then given by

$$\frac{\partial}{\partial t}(\alpha_i) + \nabla \cdot (\alpha_i \mathbf{u}) = 0. \tag{2}$$

The momentum conservation equation is expressed by

$$\frac{\partial(\rho \boldsymbol{u})}{\partial t} + \nabla \cdot (\rho \boldsymbol{u} \otimes \boldsymbol{u}) = -\nabla p + \nabla \cdot [\mu(\nabla \mathbf{u} + \nabla^{\mathrm{T}} \mathbf{u})] + \rho \mathbf{g} + \mathbf{F}_\sigma, \tag{3}$$

where $\mathbf{u}$ is the velocity vector, p is the pressure, t is the time, $\mathbf{g}$ is the gravitational acceleration vector and $\mathbf{F}_\sigma$ is the surface tension model [33] for an interfacial flow with two fluids (components). In Eqs. (4) and (5), the density and

dynamic viscosities of each component a, w are given as ρ_a, ρ_w and μ_a, μ_w, respectively, and the bulk density and dynamic viscosity are respectively expressed as

$$\rho = \alpha_a \rho_a + \alpha_w \rho_w \tag{4}$$

and

$$\mu = \alpha_a \mu_a + \alpha_w \mu_w. \tag{5}$$

The surface tension force $\mathbf{F}_\sigma$ in Eq. (3) is modeled through the continuum surface force (CSF) method [33] as

$$\mathbf{F}_\sigma = \sigma \kappa \tilde{\mathbf{n}} \delta, \tag{6}$$

where σ denotes the (constant) suface tension, κ is the interfacial curvature, $\tilde{\mathbf{n}}$ is the interfacial unit normal, and δ is the Dirac delta function. We further represent δ as $|\nabla \alpha|$ and $\tilde{\mathbf{n}}$ as $\frac{\nabla \alpha}{|\nabla \alpha|}$ which reformulates the CSF based on the component volume fraction and gives the surface tension force as

$$\mathbf{F}_\sigma = \kappa \sigma \nabla \alpha. \tag{7}$$

B. Numerical method

Here, we provide a description of the numerical procedure used to carry out the computations. We have chosen a method that employs adaptive, unstructured meshing in order to maximize the efficiency of the simulations without sacrificing their accuracy. Of the various methods used to discretize the governing equations in the literature [34,35], the finite-element method is best suited for use with unstructured meshes [36]. We have chosen the volume-of-fluid method [37] over other techniques [38–40] because of its distinct advantages of mass conservation, easy representation of arbitrary shaped interfaces, natural handling of large deformations, interface rupture, and coalescence. Temporal discretization was carried out using the second-order Crank-Nicolson method due to its simplicity and accuracy [35,40].

The numerical code uses a mixed, control-volume and finite-element formulation to discretize the Navier-Stokes equations. The main numerical framework includes a finite-element-type velocity-pressure element pair (P1DG-P2) for multifluid flow problems, which ensures exact balance between buoyancy force and pressure gradient and also ensures stability in the obtained solution. The framework also features an interface capturing scheme based on a compressive control-volume advection method [41]. The implementation of capillary forces in this framework using a balanced-force surface tension method on an unstructured mesh minimizes spurious velocities often found in interfacial flows [42]. Finally, use of anisotropic unstructured mesh adaptivity [43] allows the grid resolution to be concentrated in relatively important regions, such as the vicinity of interfaces, while lower resolution can be used in other regions.

C. Numerical setup

The high density ratio (about 889) associated with the water-air systems considered, coupled with the thinness of the film, renders the simulations challenging, thereby necessitating a long computational domain to capture the details of the interaction between the waves. The computational domain dimensions used here are $[0,600h_N] \times [-h_N, 3h_N]$ where h_N is the Nusselt film thickness for a flat film [44] (see Table I). The x and y axes are oriented in the streamwise and wall-normal directions, respectively. The y range is $-h_N < y < 3h_N$, so the undisturbed interface is at $y = 0$.

The overall computational domain is initially discretized by 1500×40 layers, with the mesh made uniform in the x (streamwise) direction, with a mesh size of $0.4h_N$. A mesh size of $0.1h_N$ is, however, used in the wall-normal y direction,

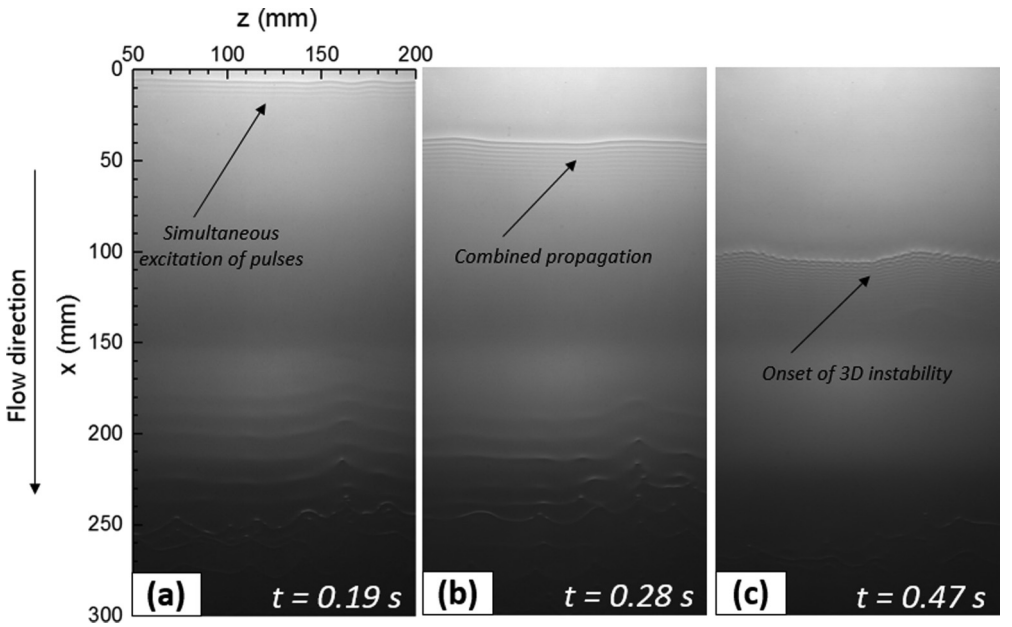

FIG. 3. Shadowgraphic images showing the evolution and propagation of the pulse waves in the solitary wave behavior mode. The snapshots in (a–c) have been captured at 0.19, 0.28, and 0.47 s, respectively. The parameter values are $\mathrm{Re} = 111, \mathrm{We} = 4.27, \beta = 5^\circ, A = 0.04\,\mathrm{s}, B = 0.04\,\mathrm{s}$, and $T = 0.08\,\mathrm{s}$. See the Supplemental Material [46], Movie 1.

from $[-h_N,\ 0.5h_N]$ which allows us to increase gradually to the end in the y domain as necessary. Mesh adaptivity based on the volume fraction field was employed during the simulation in order to save the computational effort. A no-slip boundary condition is enforced at both the substrate surface and the upper boundary of the y domain, while the zero gradient boundary condition is applied at the outlet in the x direction. The outlet is treated thus to ensure that the waves leave the computational domain without distortion of the upstream flow [45]. Essentially, this is implemented by imposing no mathematical conditions on the outflow nodes but treating them as unknowns.

At the inlet, $x = 0$, a parabolic velocity profile is imposed for the liquid film:

$$U_{\text{in}}(y \leqslant 0) = \frac{3}{2}\left(1 - \left(\frac{y}{h_N}\right)^2\right)u_p, \tag{8}$$

where U_{in} is the velocity in the film flow; u_p is the mean velocity with regards to the pulsation effect (and expressed in relation to the Nusselt estimate of film velocity). The velocity for the air phase at the inlet is set as

$$U_{\text{in}}(y > 0) = \frac{3}{2}\left(1 - \left(\frac{y}{3h_N}\right)^2\right)u_p. \tag{9}$$

The air flow in the simulation plays a passive role. The film is taken to be initially flat, and the pulse-wave excitation velocities are introduced via the variation of u_p according to the following relations:

$$u_p = \begin{Bmatrix} u_N & t \leqslant t_0 \\ 2 \times u_N & t_0 < t \leqslant (t_0 + A) \\ u_N & (t_0 + A) < t \leqslant (t_0 + A + B) \\ 2 \times u_N & (t_0 + A + B) < t \leqslant (t_0 + 2A + B) \\ u_N & t > (t_0 + 2A + B) \end{Bmatrix}, \tag{10}$$

where u_N is the Nusselt velocity.

For a close comparison between the experimental and numerical results, the parameters were matched carefully. The parameter t_0 which denotes the time interval of natural film development prior to pulse-wave excitation (see Fig. 2) was fixed at 0.1 s throughout the experimental runs and numerical computations. Parameter A, the pulsation time, was fixed at 0.04 s, and B, the interpulse interval, was varied in the range 0.04–0.12 s. Due to the computational time requirements for each experimental case studied (a total of 540 experimental data points on the average of 5), only a limited number of cases were simulated for each interaction mode in order to

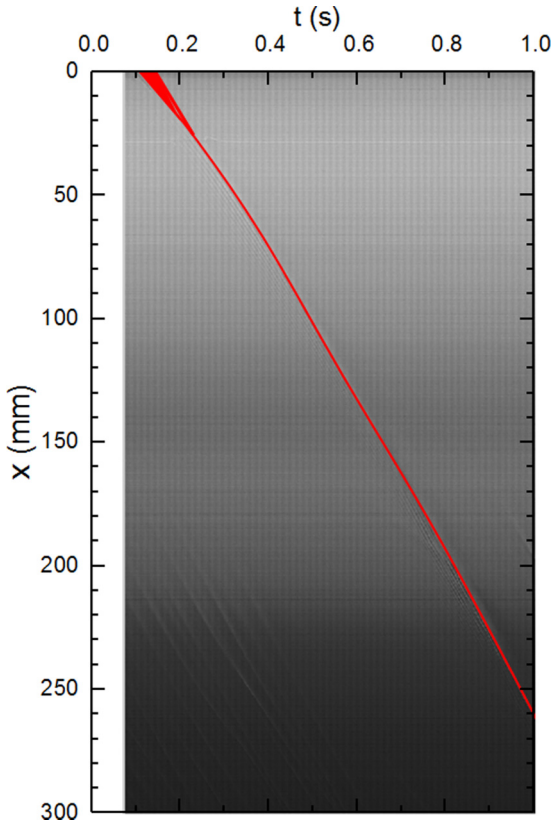

FIG. 4. Space-time plot obtained from high-speed images for the parameters in Fig. 3. The propagation line of the wave hump has been highlighted here for emphasis.

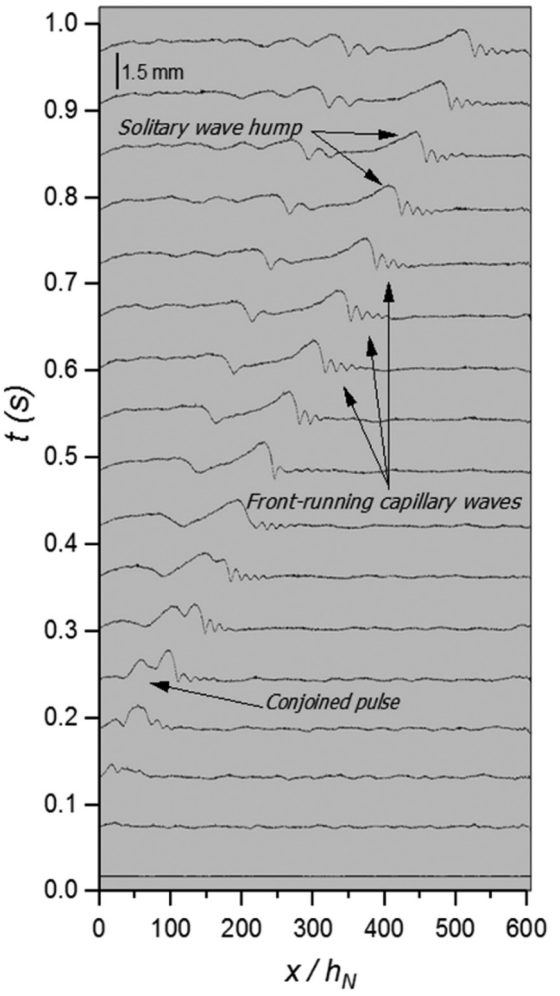

FIG. 5. Numerical results showing computed spatiotemporal propagation of doubly excited pulse waves in the solitary wave behavior mode at 0.06 s interval. The parameters here correspond to those used to generate Fig. 3. See the Supplemental Material [46], Movie 2.

compare the predictions both quantitatively and qualitatively with experimental observations.

IV. RESULTS AND DISCUSSION

In this section, a discussion of our experimental results is provided. The various interaction patterns obtained are shown and described in detail. An in-depth analysis of the effect of film flow rate, interpulse interval, and substrate inclination angle on the merging distance of these binary pulses is also provided for the "coalescence" mode. Comparisons of the experimental results with numerical predictions are also discussed. The section concludes with a regime map showing the pattern transition in the parameter space.

A. Solitary wave mode

Prior to pulse-wave excitation, the film surface is populated by naturally developing waves, which are formed as a result of disturbance amplification at the film inlet, that grow gradually into two- and then three-dimensional solitary waves. Previous studies on flowing liquid films have shown that the amplitude of these naturally forming waves is much smaller than that of excited pulse waves [23]. In order to describe the spatiotemporal dynamics of the pulse waves, space-time graphs were plotted for each experimental case. The wave speeds were estimated from the gradient of the pulse-wave lines. The time duration for the study of the wave interactions in both the experiment and simulation was limited to 0.9 s with a duration of 0.1 s allowed for the preevolution of naturally developing waves on the film. These can be noticed from the space-time plots with the regular emergence of the first pulse at time $t = 0.1$ s.

The first mode of interaction of the doubly excited pulse waves is the "solitary behavior mode." An example of this is shown in Fig. 3, which corresponds to $\mathrm{Re} = 111, \mathrm{We} = 4.27$, an inclination angle of 5°, a and pulse interval of 0.04 s. In this mode, the pulse waves are observed to appear conjoined on the film surface, prior to their evolution into a solitary wave structure. In the first snapshot [Fig. 3(a)], there is an

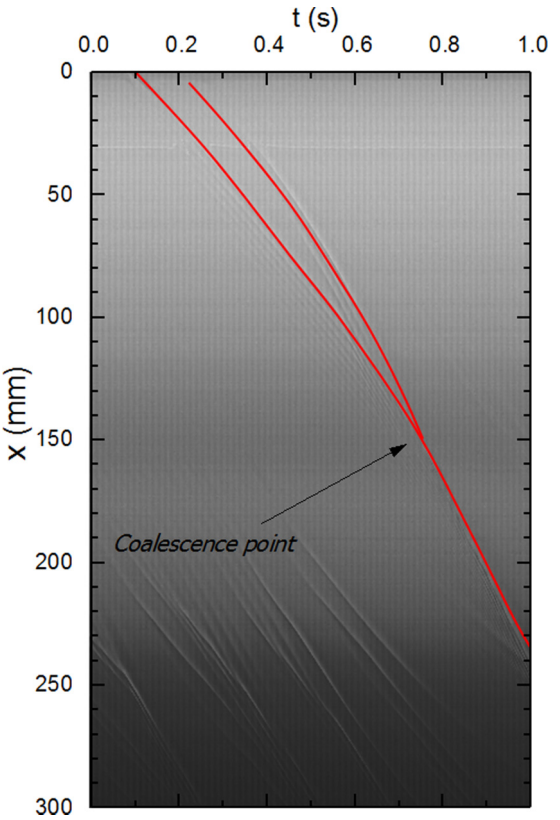

FIG. 7. Space-time plot obtained from high-speed images. The propagation lines of the wave humps have been thickened here for emphasis.

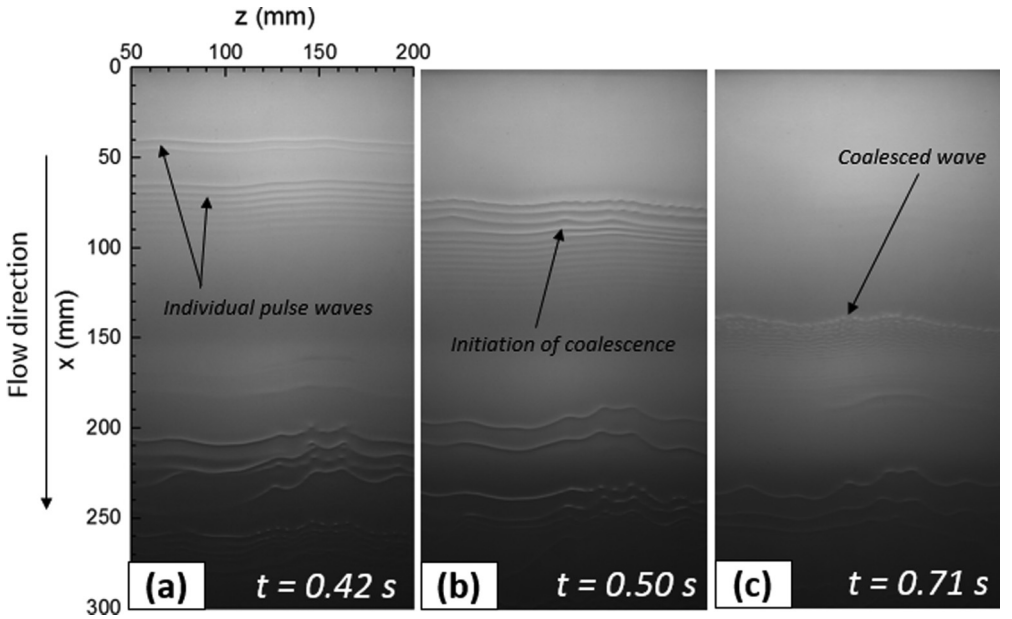

FIG. 6. Shadowgraphic images showing the evolution and propagation of the pulse waves in the complete pulse coalescence mode. The snapshots in (a–c) have been captured at 0.42, 0.50, and 0.71 s, respectively. The parameter values are $\mathrm{Re} = 83.3, \mathrm{We} = 5.47, \beta = 10°, A = 0.04\,\mathrm{s}, B = 0.08\,\mathrm{s}$, and $T = 0.12\,\mathrm{s}$. See the Supplemental Material [46], Movie 3.

appearance of a singular hump pulse wave, which gradually develops into a full solitary wave structure as it propagates downstream [Figs. 3(b) and 3(c)]. The simultaneous appearance of this wave suggests an insufficient space for growth of individual solitary waves, which forces both pulses to merge into a single one.

Although efforts were geared towards ensuring the interactions were focused solely on two-dimensional waves by restricting the inclination angles to low values, the development of three-dimensional instabilities could not be eliminated completely. These instabilities, however, did not grow on a sufficiently short time scale so as to influence the results for inclination angles between 5° and 15°; this ensured that the wave interactions are captured for two-dimensional waves for a considerable length of film surface before the waves significantly yield to three-dimensional instabilities. We note that this limitation has been predicted in previous work [6,30,47].

The propagation of this combined pulse wave is as shown in the space-time plot depicted in Fig. 4. From this plot, a single propagation line is highlighted for the combined wave. The appearance of a thicker propagation line at the inlet confirms the observation of the conjoined behavior of the pulses. The gradient of this line was used to calculate the speed of these merged pulses which was found to be 0.321 m/s; this is larger than that of the individual pulses, 0.228 m/s. This indicates that the merger of the pulse waves has led to an increase in speed of the combined pulses.

The computed spatiotemporal propagation of the pulses is shown in Fig. 5. The consecutive free-surface profile has been superimposed and the results are shown every 0.06 s. An inspection of the results presented reveals that the flow regime observed experimentally is also captured by the numerical simulations of the two-dimensional Navier-Stokes equations. However, we observe here what is not apparent in the shadowgraphic images. Essentially, the simulation results show an ongoing merger between the two pulse waves, which leads to a conjoined pulse hump, which then travels as a single, coherent structure that grows into a singular solitary waveform. The x-t plot in Fig. 4 also reveals this through the thickness of the propagation line at the substrate inlet.

In the propagation of this solitary wave, the front-running capillary waves generate negative capillary pressure, which drains out liquid from the crest and due to this resists a further steepening of the solitary hump as a result of gravitational pull. This explains qualitatively the maintenance of the shape of a solitary pulse wave in the singular behavior mode. This is in agreement with the predictions of Vlachogiannis and Bontozoglou [48]. The computed speed of the singular solitary waveform in the simulation was found to be 0.324 m/s, which is in agreement with the experimental value, 0.321 m/s. This "solitary mode" behavior is observed to be chiefly favored by low interpulse time spacing and low substrate inclination angles.

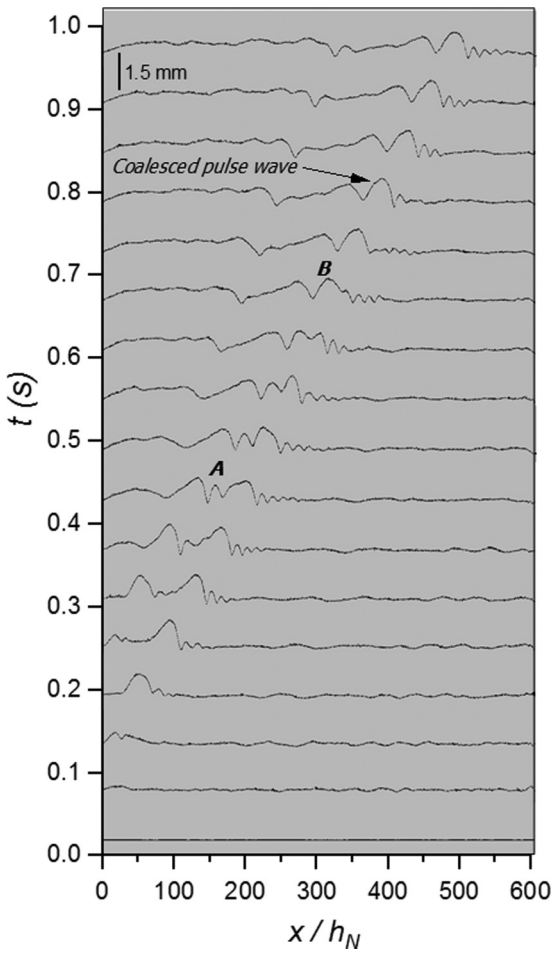

FIG. 8. Numerical results showing computed spatiotemporal propagation of doubly excited pulse waves in the coalescence mode with 0.06 s interval. The parameters here correspond to those used to generate Fig. 6. The points labeled A and B show the onset and completion of coalescence, respectively. See the Supplemental Material [46], Movie 4.

B. Coalescence mode

The second mode of interaction of the doubly excited pulse waves is the coalescence mode shown in Fig. 6.

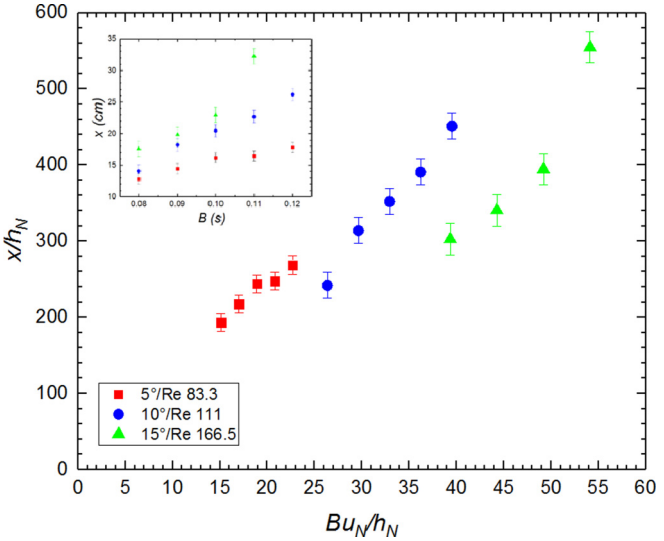

FIG. 9. Variation of the coalescence point with the pulse interval in the coalescence mode, expressed in dimensionless variables. The red, blue, and green points trace the coalescence points at substrate inclination angles of 5°, 10°, and 15°, respectively. The pulse duration, A has been maintained at 0.04 s. The inset is a dimensional plot of coalescence point against dimensional pulse interval.

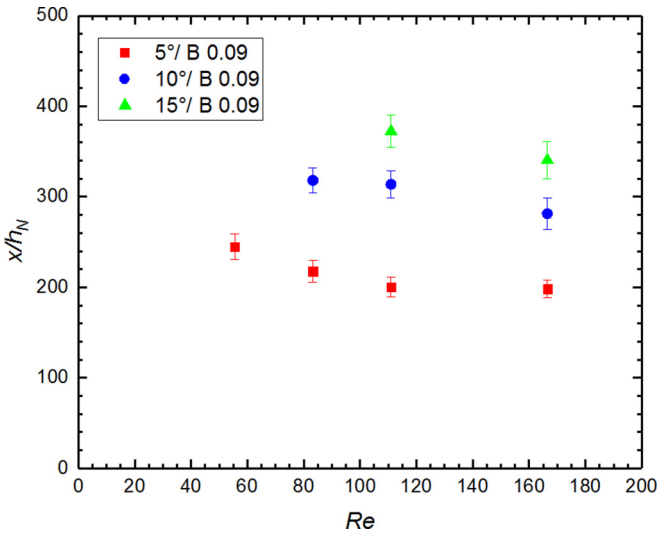

FIG. 10. Variation of the coalescence point with the Reynolds number for different substrate inclination angles: 5°, 10°, and 15° at a constant interpulse interval.

This corresponds to wave interactions for a film with Re = 83.3, We = 5.47, an inclination angle of 10°, and an interpulse time spacing of 0.08 s. Here, a distinct interaction mode from the solitary mode discussed previously is seen. We observe that the binary pulses appear distinctly on the film surface [Fig. 6(a)] and grow into full and independent solitary waves, which are identified by a main hump and a series of front-running capillary waves. They also travel separately on the film surface and only later coalesce [Fig. 6(b)] into a single wave. In the snapshot in Fig. 6(a), the individual pulse waves are captured with the preceding pulse already developed into a complete solitary waveform, with the characteristic main hump and series of front-running bow waves, and the trailing pulse in the evolution process. The initiation of the coalescence is captured in Fig. 6(b). This interaction is observed to be triggered by the attachment of the capillary ripples of the trailing solitary pulse wave to the tail of the leading one. The initiated attachment process slows down the leading pulse, thereby facilitating a steady decrease in the separation distance between them (see Fig. 7). A modulation of the tail of the preceding pulse is experienced, which ensures that liquid drains from the trailing pulses that lead to the growth of the hump of the leading pulse. This capillary effect induced by the front-running ripples of the second pulse leading to a differential pressure, which drains liquid out of the tail of the trailing pulse, has also been detailed by Malamataris *et al.* [47]. This attachment process becomes complete when both pulses finally travel with a single main hump and share a series of front-running capillary waves before them [Fig. 6(c)].

The scenario described above can also be seen clearly in the numerical simulations shown in Fig. 8. The combined wave speed and coalescence point were computed numerically to be 0.402 m/s and 0.155 m, in comparison to their experimental counterparts of 0.398 m/s and 0.149 m, respectively. This shows good agreement between the experimental and numerical results.

The coalescence point between these binary pulse waves is also examined as a function of Re, interpulse interval, and the substrate inclination angle. In order to generalize the conclusions drawn from our results, we express our findings in terms of dimensionless space, $(x,y)/h_N$; velocity, $\mathbf{u}/u_N$,; an time, tu_N/h_N. A plot of the dimensionless coalescence point against the pulse interval in the coalescence mode is shown in Fig. 9. It can be seen that the coalescence distance increases with interpulse time spacing. This can be seen at the different substrate inclination angles. However, it can be noticed that this increase becomes particularly accentuated at the highest

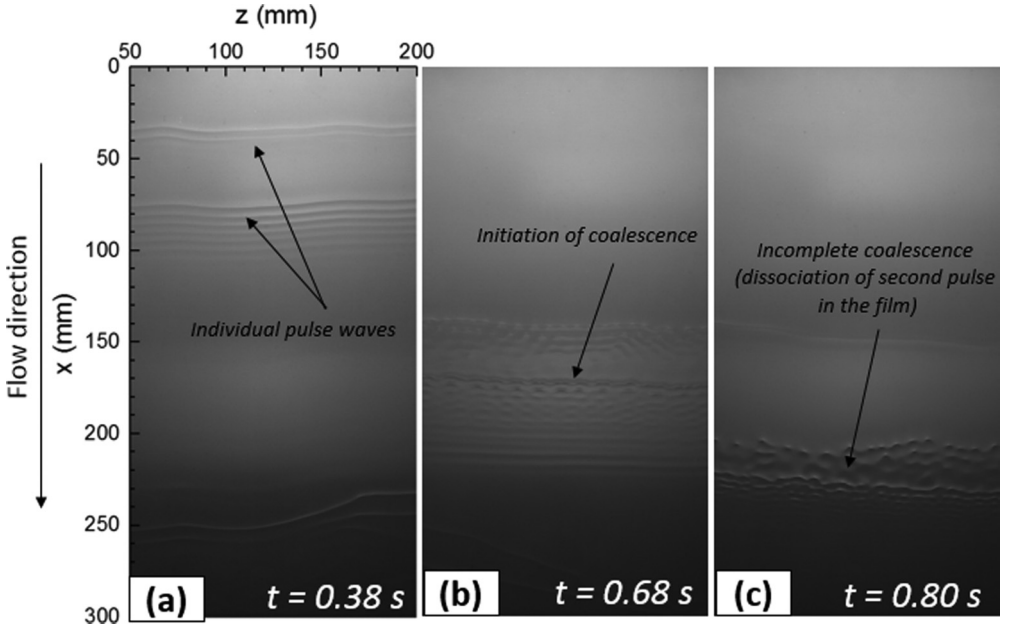

FIG. 11. Shadowgraphic images showing the evolution and propagation of the pulse waves in the partial coalescence mode. The snapshots in (a–c) have been captured at 0.38, 0.68, and 0.80 s, respectively. The parameter values are Re = 83.3, We = 5.47, $\beta = 10°$, $A = 0.04$ s, $B = 0.12$ s, and $T = 0.16$ s. See the Supplemental Material [46], Movie 5.

inclination angle. This is to be expected since the wave speed increases with substrate inclination. From Fig. 10, we can also see that the coalescence distance is a decreasing function of Re, and increases with inclination angle for a fixed value of Re. This is in agreement with the findings of Vlachogiannis and Bontozoglou [48] that the coalescence point and coalescing time of two interacting solitary waves increase as the film speed is reduced.

C. Partial coalescence mode

Another type of behavior exhibited by the pulses is revealed in Fig. 11 which corresponds to interactions at film $\mathrm{Re} = 83.3, \mathrm{We} = 5.47$, an inclination angle of 10°, and an interpulse spacing of 0.12 s. The two pulses appear at the onset as separate humps, which propagate on the film surface, eventually developing into full, independent solitary waves [Fig. 11(a)]. As in the coalescence mode, the attachment process between the pulses also commences [Fig. 11(b)] but here, the distinguishing factor is that the attachment process is short-lived and never reaches completion [Fig 11(c)]; instead, the hump of the second solitary pulse is observed to be cut off from its capillary ripples and travels disconnected from the first pulse or gets dissipated in the film [Fig. 11(c)]. This disconnected hump is highlighted in the space-time plot (Fig. 12) as a separately propagating waveform. Hence two separate solitary humps are seen at the end of the interaction with only the first one possessing front-running capillary waves while the second remains as an isolated wave hump.

We observe in cases where a third pulse was excited (in a multiple excited pulses scenario) that this disconnected solitary hump realigns itself with the oncoming wave, thereby resulting in another inelastic collision. Though we have chosen to limit the discussion of our results to the events occurring between binary waves, we consider that the interaction patterns between multiple pulse waves may provide further rich and interesting insight into the nature of solitary wave interactions.

We observe the mode of interaction described above to occur mostly at low Re values as well as moderate to wide interpulse spacing. It is assumed that the low propagation speed of the trailing hump is the main reason for this mode of interaction. Because of the incompleteness of the process of attachment, this interaction mode is termed "partial coalescence." A similar scenario has been captured in the numerical simulations shown in Fig. 13. The entrance of each pulse wave is observed by an elevation of the liquid level at the inlet of the domain, while each pulse develops into a solitary wave structure as it propagates on the film surface. As the process of merging begins, the leading hump experiences growth in its amplitude while the trailing pulse

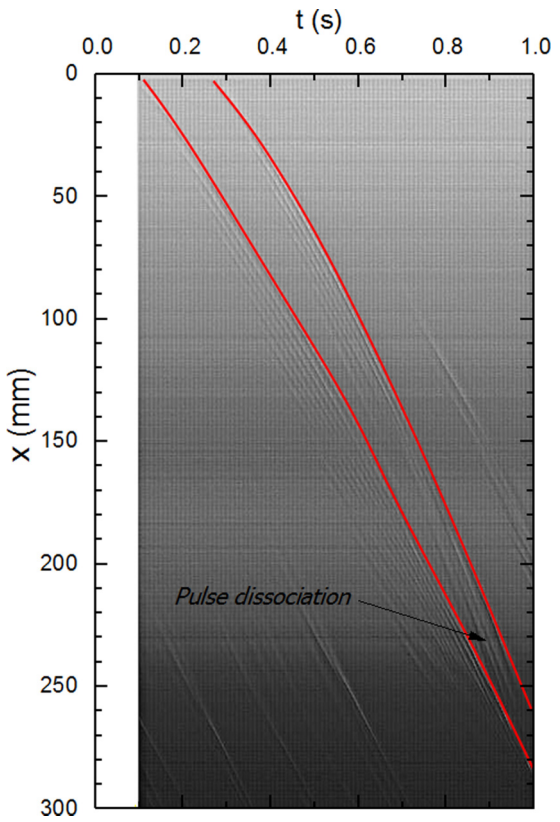

FIG. 12. Space-time plot obtained from high-speed images. The propagation lines of the wave humps have been thickened here for emphasis.

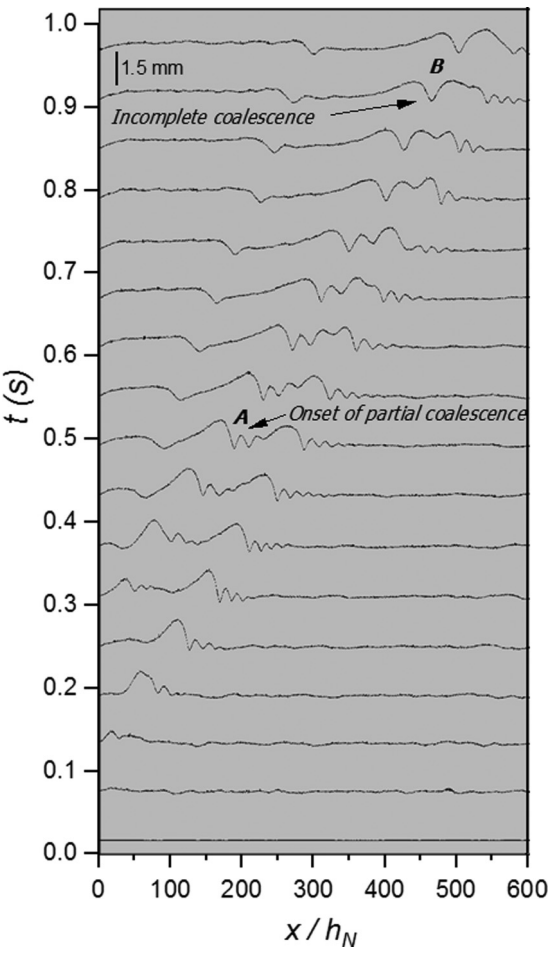

FIG. 13. Numerical results showing computed temporal propagation of doubly excited pulse waves in the partial coalescence mode at 0.06 s interval. The parameters here correspond to those used to generate Fig. 11.

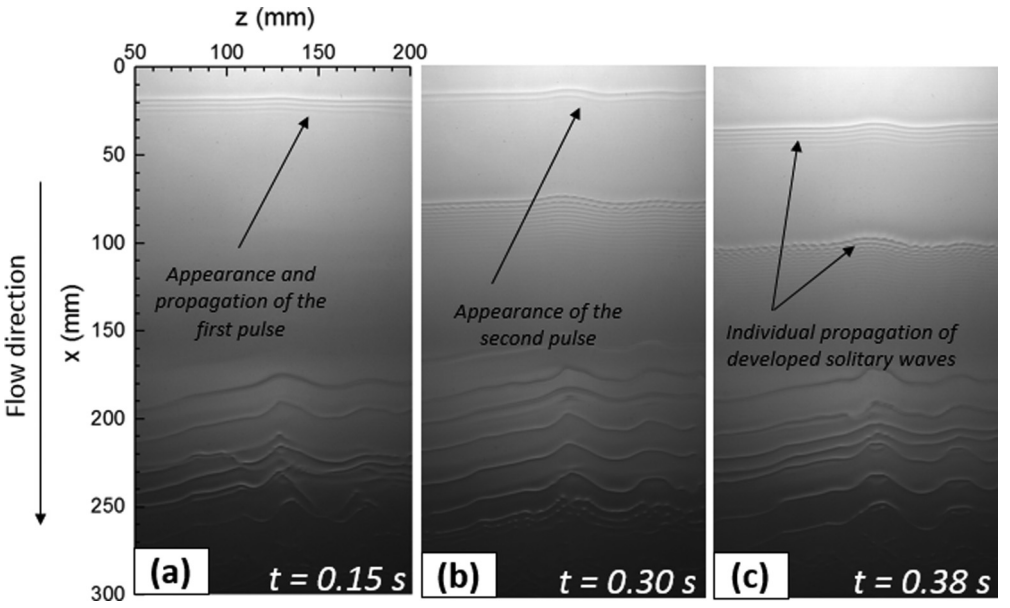

FIG. 14. Shadowgraphic images showing the evolution and propagation of the pulse waves in the total noncoalescence mode. The snapshots in (a–c) have been captured at 0.15, 0.30, and 0.38 s, respectively. The parameter values are $\mathrm{Re} = 83.3, \mathrm{We} = 4.79, \beta = 15^\circ, A = 0.04\,\mathrm{s}, B = 0.12\,\mathrm{s}$, and $T = 0.16\,\mathrm{s}$. See the Supplemental Material [46], Movie 7.

decreases steadily (with a decay rate that is linear in space but exponential in time). However, unlike the case in the complete coalescence mode, a more prominent hump is still observed after the merging process (see the point labeled B in Fig. 13), which agrees with the experimental observation of a disconnection between the hump and capillary ripples of the second pulse during the merger process. The leading pulse speed was measured to be 0.355 m/s in the experiment and computed to be 0.360 m/s numerically, thereby showing the good agreement between both the experiment and numerical simulation. See the Supplemental Material [46], Movie 6.

D. Pulse noncoalescence

Here, we discuss the final, distinct mode of flow behavior observed in this study. Figure 14 shows the pulse-wave interactions on a film with $\mathrm{Re} = 83.3, \mathrm{We} = 4.79$, an inclination angle of 15°, and an interpulse spacing 0.12 s. From the first snapshot [Fig. 14(a)], the leading pulse appears distinctly and immediately commences its growth and development into a full solitary wave structure, while the trailing pulse follows soon afterwards [Fig. 14(b)]. These pulses are observed to travel separately, with the characteristic features of a fully developed solitary wave, i.e., a large hump with a series of front-running capillary ripples, just as in the previous two modes (Figs. 6 and 11). Their distinct noninteracting propagation lines are shown in the space-time plot (Fig. 15).

As observed in Fig. 14, there is no attachment process initiated between these traveling pulses; hence they never coalesce. Instead, an essentially constant spacing of a clear flat film which separates both waves is attained between the two pulses after their development into full solitary waves [Fig. 14(c)] and remains unchanged throughout their propagation. This constant separation distance has been found to increase with the initial pulse time spacing. The convergence of the traveling interacting solitary wave to bound states at large separation distance has also been predicted by Chang *et al.* [25], Tseluiko *et al.* [26], and Pradas *et al.* [27].

This dynamics and the formation of the bound-state-like structures are also well captured by the numerical simulations

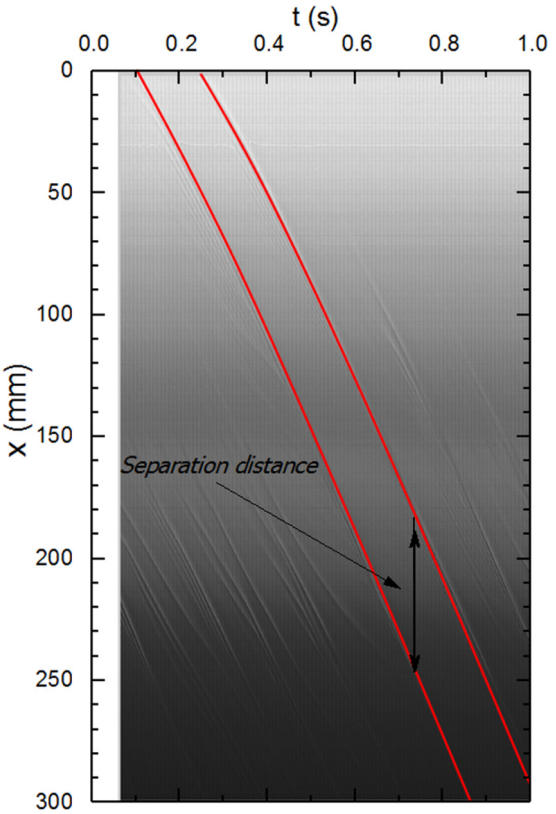

FIG. 15. Space-time plot obtained from high-speed images. The propagation line of the wave humps have been thickened here for emphasis.

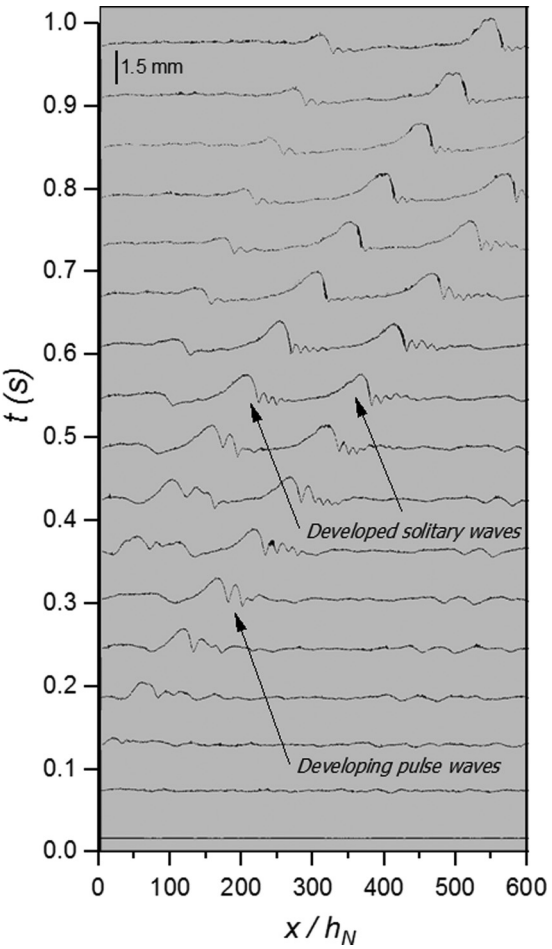

FIG. 16. Numerical results showing computed temporal propagation of doubly excited pulse waves in the pulse noncoalescence mode at 0.06 s interval. The parameters used correspond to those used to generate Fig. 14. See the Supplemental Material [46], Movie 8.

(Fig. 16). The pulse-wave speeds were measured to be 0.403 m/s in the experiments and computed to be 0.406 m/s numerically. Similarly, the separation distance between the two pulses was measured to be 0.067 m in the experiment and found to be 0.068 m in the numerical simulation.

E. Regime map of pulse-wave interactions

A regime map of the different interaction modes between these binary excited pulses is shown in Fig. 17. This map gives a representation of the characteristic effect of the different parameters studied (i.e., film flow rate, interpulse interval, and substrate inclination angle) on the modes of interaction between these pulses. As can be seen, the solitary mode behavior is favored chiefly by low interpulse time spacing and by low substrate inclination angles; the coalescence mode, on the other hand, is seen to occur for low inclination angles and moderate interpulse spacing. The partial coalescence mode is observed at low film flow rates and low inclination angle, while the "total noncoalescence mode" is favored by high inclination angles, and high interpulse time spacing.

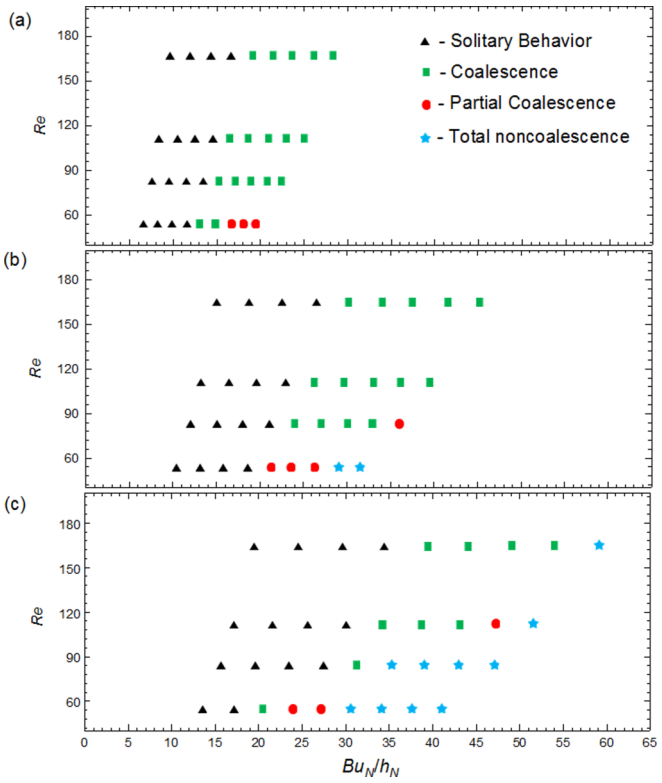

FIG. 17. Flow regime map of the pulse-wave interactions based on the film Re and dimensionless interpulse interval at 5°, 10°, and 15° corresponding to (a–c), respectively. The black triangle, green square, red circle, and blue star represent the different interaction modes which are solitary mode, coalescence, partial coalescence, and total noncoalescence, respectively.

V. CONCLUSION

In this paper, the interaction patterns exhibited by doubly excited pulse waves on a flowing liquid film have been studied. The results obtained show four distinct interaction patterns, namely, solitary behavior, coalescence, partial coalescence, and total noncoalescence. It was observed that the solitary behavior occurs due to insufficient solitary wave formation length, hence the inability of the two pulses to independently develop into full isolated solitary waves. However, when the two solitary pulses are able to develop into full independent solitary waves, and the initiated process of pulse attachment between them reaches completion, coalescence or partial coalescence is observed. However, if the pulses develop into full solitary waves without an attachment process initiated between them but a constant separation length is maintained, then the interaction is referred to as pulse noncoalescence. These results confirm the predictions of Liu and Gollub [6], Tseluiko *et al.* [26], and Pradas *et al.* [27] that solitary humps with sufficiently large separation distance experience repulsion of the humps until a steady bound state is achieved between them; humps separated by smaller distances experience attraction leading to an inelastic collision and coalescence.

The different factors responsible for each of these interaction modes have also been considered in detail. These include low interpulse time spacing as well as low substrate inclination angle for the singular behavior mode, while low film flow rate

and low substrate inclination angle favor partial coalescence. The total noncoalescence mode, however, is enhanced with high inclination angles and high interpulse time spacing. A regime map to indicate the phases of appearance of these individual interaction patterns was also plotted based on the film flow rate and the interpulse time spacing.

The effect of system parameters on the coalescence point of these binary waves in the coalescence mode has also been studied and the results show that an increase in the film flow rate led to a slight decrease in the coalescence point while both substrate inclination angle and interpulse interval led to an increase of the coalescence point of these pulse waves. Of these two parameters, the interpulse interval was found to have a more significant effect. Finally, the complete scenario was numerically simulated by the artificial introduction of pulse waves at the computational inlet and results show good agreement with the experimental data.

ACKNOWLEDGMENTS

We would like to acknowledge the financial support of the Petroleum Technology Development Fund (Ptdf, Nigeria) as well as the Engineering and Physical Sciences Research Council, UK, through the Programme Grant MEMPHIS (Grant No. EP/K003976/1).

[1] H. A. Stone, A. D. Stroock, and A. Ajdari, Annu. Rev. Fluid Mech. **36**, 381 (2004).
[2] D. P. Frisk and E. J. Davis, Int. J. Heat Mass Transfer **15**, 1537 (1972).
[3] P. N. Yoshimura, T. Nosoko, and T. Nagata, Chem. Eng. Sci. **51**, 1231 (1996).
[4] R. V. Craster and O. K. Matar, Rev. Mod. Phys. **81**, 1131 (2009).
[5] P. L. Kapitza and S. P. Kapitza, J. Exp. Theor. Phys. **19**, 105 (1949).
[6] J. Liu and J. P. Gollub, Phys. Fluids **6**, 1702 (1994).
[7] J. Liu, J. B. Schneider, and J. P. Gollub, Phys. Fluids **7**, 55 (1995).
[8] C. D. Park and T. Nosoko, AIChE J. **49**, 2715 (2003).
[9] T. Nosoko, P. N. Yoshimura, T. Nagata, and K. Oyakawa, Chem. Eng. Sci. **51**, 725 (1996).
[10] T. Nosoko and A. Miyara, Phys. Fluids **16**, 1118 (2004).
[11] N. Kofman, S. Mergui, and C. Ruyer-Quil, J. Fluid Mech. **757**, 854 (2014).
[12] C. S. Yih, in *Proceedings of the Second US Congress on Applied Mechanics* (ASME, New York, 1955).
[13] C. S. Yih, J. Fluid Mech. **31**, 737 (1968).
[14] T. B. Benjamin, J. Fluid Mech. **2**, 554 (1957).
[15] D. J. Benney, J. Math. Phys. **45**, 150 (1966).
[16] V. Y. Shkadov, Fluid Dyn. Res. **2**, 21 (1967).
[17] H. Yu, T. Gambaryan-Roisman, and P. Stephan, J. Heat Transfer **135**, 101010 (2013).
[18] L. T. Nguyen and V. Balakotaiah, Phys. Fluids **12**, 2236 (2000).
[19] H. C. Chang and E. A. Demekhin, *Complex Wave Dynamics on Thin films* (Elsevier Science, Amsterdam, 2002).
[20] S. Kalliadasis, C. Ruyer-Quil, B. Scheid, and M. G. Velarde, *Falling Liquid Films* (Springer, Berlin, 2011).
[21] S. V. Alekseenko, V. E. Nakoryakov, and B. G. Pokusaev, *Wave Flow of Liquid Films* (Begell House, New York, 1994).
[22] S. V. Alekseenko, V. Y. Nakoryakov, and B. G. Pokusaev, AIChE J. **31**, 1446 (1985).
[23] A. Miyara, Int. J. Therm Sci. **39**, 1015 (2000).
[24] D. Gao, N. B. Morley, and V. K. Dhir, J. Comput. Phys. **192**, 624 (2003).
[25] H. C. Chang, E. A. Demekhin, and E. Kalaidin, J. Fluid Mech. **294**, 123 (1995).
[26] D. Tseluiko, S. Saprykin, C. Duprat, F. Giorgiutti-Dauphiné, and S. Kalliadasis, Phys. D (Amsterdam, Neth.) **239**, 2000 (2010).
[27] M. Pradas, S. Kalliadasis, and D. Tseluiko, IMA J. Appl. Math. **77**, 028 (2012).
[28] S. V. Alekseenko, V. E. Nakoryakov, and B. G. Pokusaev, Int. J. Multiphase Flow **11**, 607 (1985).
[29] H. C. Chang, E. A. Demekhin, and D. I. Kopelevich, J. Fluid Mech. **250**, 433 (1993).
[30] H. Chang, Annu. Rev. Fluid Mech. **26**, 103 (1994).
[31] B. Scheid, C. Ruyer-Quil, and P. Manneville, J. Fluid Mech. **562**, 183 (2006).
[32] S. V. Alekseenko and V. E. Nakoryakov, Int. J. Heat Mass Transfer **38**, 2127 (1995).
[33] J. U. Brackbill, D. B. Kothe, and C. A. Zemach, J. Comput. Phys. **100**, 335 (1992).
[34] D. Kuzmin, *A Guide to Numerical Methods for Transport Equations* (Friedrich-Alexander-Universität Erlangen-Nürnberg, Erlangen, Germany, 2010).
[35] S. C. Chapra and R. P. Canale, *Numerical Methods for Engineers* (McGraw-Hill, New York, 1998).
[36] D. R. Davies, C. R. Wilson, and S. C. Kramer, Geochem., Geophys., Geosyst. **12**, Q06001 (2011).
[37] C. W. Hirt and B. D. Nichols, J. Comput. Phys. **39**, 201 (1981).
[38] F. H. Harlow and J. E. Welch, Phys. Fluids **8**, 2182 (1965).
[39] M. Sussman, P. Smereka, and S. Osher, J. Comput. Phys. **114**, 146 (1994).
[40] G. Tryggvason, R. Scardovelli, and S. Zaleski. *Direct Numerical Simulations of Gas–Liquid Multiphase Flows* (Cambridge University Press, Cambridge, 2011).
[41] D. Pavlidis, J. L. Gomes, Z. Xie, J. R. Percival, C. C. Pain, and O. K. Matar, Int. J. Numer. Methods Fluids **80**, 256 (2015).
[42] Z. Xie, D. Pavlidis, P. Salinas, J. R. Percival, C. C. Pain, and O. K. Matar, Comput. Fluids **138**, 38 (2016).
[43] C. C. Pain, A. P. Umpleby, C. R. de Oliveira, and A. J. Goddard, Comput. Methods Appl. Mech. Eng. **190**, 3771 (2001).
[44] W. Nusselt, Z. Ver. Deutsch. Ing. **60**, 541 (1916).
[45] J. Tihon, K. Serifi, K. Argyriadi, and V. Bontozoglou, Exp. Fluids **41**, 79 (2006).
[46] See Supplemental Material at http://link.aps.org/supplemental/10.1103/PhysRevE.96.013118 for eight movies of doubly excited pulse waves on thin liquid films flowing down an inclined plane.
[47] N. A. Malamataris, M. Vlachogiannis, and V. Bontozoglou, Phys. Fluids **14**, 1082 (2002).
[48] M. Vlachogiannis and V. Bontozoglou, J. Fluid Mech. **435**, 191 (2001).